Acta Oceanol. Sin., 2018, Vol. 37, No. 9, P. 67–81
DOI: 10.1007/s13131-018-1265-6
http://www.hyxb.org.cn
E-mail: hyxbe@263.net

Smectite formation in metalliferous sediments near the East Pacific Rise at 13°N

RONG Kunbo[1, 3], ZENG Zhigang[1, 2, 3*], YIN Xuebo[1], CHEN Shuai[1], WANG Xiaoyuan[1], QI Haiyan[1], MA Yao[1]

[1] Seafloor Hydrothermal Activity Laboratory of the Key Laboratory of Marine Geology and Environment, Institute of Oceanology, Chinese Academy of Sciences, Qingdao 266071, China

[2] Laboratory for Marine Mineral Resources, Qingdao National Laboratory for Marine Science and Technology, Qingdao 266071, China

[3] University of Chinese Academy of Sciences, Beijing 100049, China

Received 14 August 2017; accepted 20 October 2017

Abstract

A 43 cm long E271 sediment core collected near the East Pacific Rise (EPR) at 13°N were studied to investigate the origin of smectite for understanding better the geochemical behavior of hydrothermal material after deposition. E271 sediments are typical metalliferous sediments. After removal of organic matter, carbonate, biogenic opal, and Fe-Mn oxide by a series of chemical procedures, clay minerals (<2 μm) were investigated by X-ray diffraction, chemical analysis and Si isotope analysis. Due to the influence of seafloor hydrothermal activity and close to continent, the sources of clay minerals are complex. Illite, chlorite and kaolinite are suggested to be transported from either North or Central America by rivers or winds, but smectite is authigenic. It is enriched in iron, and its contents are highest in clay minerals. Data show that smectite is most likely formed by the reaction of hydrothermal Fe-oxyhydroxide with silica and seawater in metalliferous sediments. The Si that participates in this reaction may be derived from siliceous microfossils (diatoms or radiolarians), hydrothermal fluids, or detrital mineral phases. And their δ^{30}Si values are higher than those of authigenic smectites, which implies that a Si isotope fractionation occurs during the formation because of the selective absorption of light Si isotopes onto Fe-oxyhydroxides. Sm/Fe mass ratios (a proxy for overall REE/Fe ratio) in E271 clay minerals are lower than those in metalliferous sediments, as well as distal hydrothermal plume particles and terrigenous clay minerals. This result suggests that some REE are lost during the smectite formation, perhaps because their large ionic radii of REE scavenged by Fe-oxyhydroxides preclude substitution in either tetrahedral or octahedral lattice sites of this mineral structure, which decreases the value of metalliferous sediments as a potential resource for REE.

Key words: metalliferous sediments, smectite formation, REE, silicon isotope

Citation: Rong Kunbo, Zeng Zhigang, Yin Xuebo, Chen Shuai, Wang Xiaoyuan, Qi Haiyan, Ma Yao. 2018. Smectite formation in metalliferous sediments near the East Pacific Rise at 13°N. Acta Oceanologica Sinica, 37(9): 67–81, doi: 10.1007/s13131-018-1265-6

1 Introduction

Hydrothermal metalliferous sediments are thought to be formed by either the hydrothermal non-buoyant plume fallout of Fe- and Mn-oxyhydroxide precipitates, or mass-wasting and erosion of primary submarine massive sulfides, and the hydrothermal buoyant plume fallout of Fe- and Mn-oxyhydroxides and sulfides (Dekov et al., 2010 and references therein). In addition, the plume-derived metalliferous component of these sediments is diluted by the background sedimentation of detrital and biogenic material (Mills and Elderfield, 1995). The formation mechanism of authigenic smectite and its material source in metalliferous sediments reflects the interactions between hydrothermal material and non-hydrothermal mineral phases. These are important research topics as authigenic smectite is common in a number of hydrothermal fields, including Atlantis II Deep in the Red Sea (Bischoff, 1972; Cole, 1988), the Grimsey and Kolbeinsey hydrothermal fields off the north coast of Iceland (Lackschewitz et al., 2006), the Iheya North Knoll in the Okinawa Trough (Miyoshi et al., 2015; Shao et al., 2015), in the Southeast Pacific (Heath and Dymond, 1977; Dymond and Eklund, 1978), in the Galapagos hydrothermal mound field of the Galapagos Spreading Center (Rateev et al., 1980; Barrett et al., 1983; Honnorez et al., 1983), along the Juan de Fuca Ridge (JdFR) (Percival and Ames, 1993; Zierenberg and Shanks III, 1994), and on the East Pacific Rise (EPR) near 21°N (Alt et al., 1987; Alt, 1988). Although the authigenic smectite at these sites has different origins, these minerals are thought to be related to seafloor hydrothermal activity.

The EPR at 13°N is an area of intense seafloor hydrothermal activity and volcanism (Hekinian et al., 1983a, b ; Hekinian and Fouquet, 1985). As a result, a field of metalliferous sediments oc-

Foundation item: The National Natural Science Foundation of China under contract No. 41325021; the National Basic Research Program (973 Program) of China under contract No. 2013CB429700; the National Special Fund for the 12th Five-Year Plan of COMRA under contract No. DY125-12-R-02; the Special Fund for the Taishan Scholar Program of Shandong Province under contract No. ts201511061; the AoShan Talents Program Supported by Qingdao National Laboratory for Marine Science and Technology under contract No. 2015ASTP-0S17.

*Corresponding author, E-mail: zgzeng@ms.qdio.ac.cn

curs as a series of dispersion holes of underwater hydrothermal mineral forming systems on both sides of the EPR 9°–14°N axis, characterized by high-temperature activity and massive sulfide deposits (Gurvich, 2006). Researchers have investigated the lithology and geochemistry of recent metalliferous sediments in this area (Davydov et al., 2002; Xue, 2003; Yuan et al., 2007; Yu, 2010); in particular, Gurvich (2006) found that smectite and clay minerals are the main constituents of metalliferous sediments near the East Pacific Rise (EPR) at 13°N. However, the origin of smectite and clay minerals in this area remains unclear.

This study reports new data on metalliferous sediments and clay minerals collected near the EPR at 13°N. The analysis encompasses major and trace elements and X-ray diffraction (XRD) and scanning electron microscope (SEM) and Si isotopes to discuss the origin of clay minerals and the formation mechanisms of smectite as well as the Si source, isotope fractionation, and rare earth element (REE) behavior during this process. The aim of this study was to develop a better understanding of the geochemical behavior of inputs from hydrothermal fluids subsequent to deposition as well as any possible link to smectite formation.

2 Geologic setting

The EPR at 13°N is a fast-spreading section of the global mid-ocean ridge system located between the Orozco (15°N) and Clipperton fracture zones (10°N). It is extremely linear in plan view (Fig. 1a); its full spreading rate at this latitude is approximately 100–110 mm/a (Klitgord and Mammerickx, 1982; Choukroune et al., 1984).

The EPR in this region is formed of a continuous, but asymmetric, axial topographic high that is about 8 km wide and 250 m high (Francheteau and Ballard 1983). This asymmetric axial ridge measures about 5 km from its center to the east and about 3 km

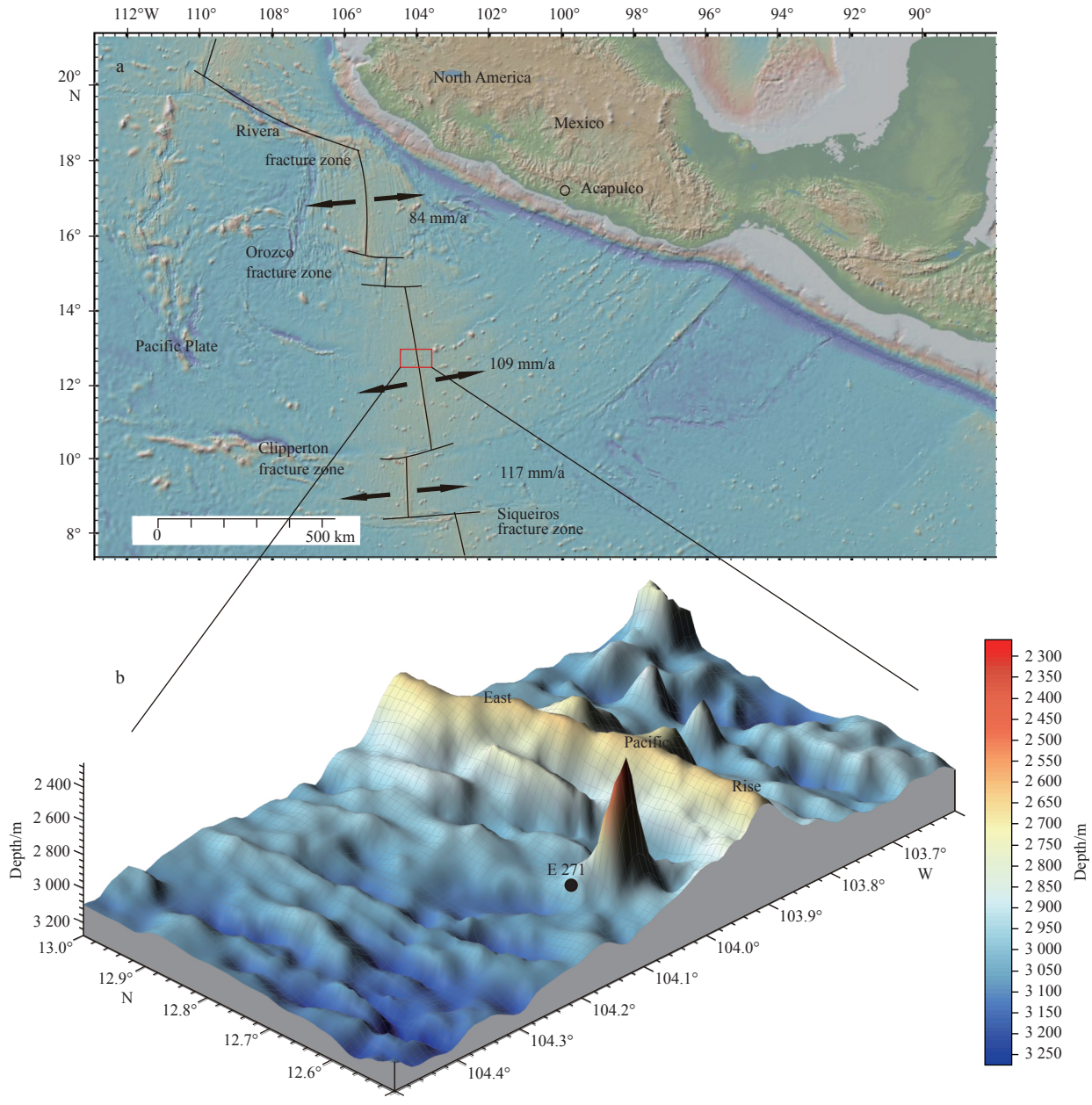

Fig. 1. Tectonic map of the study area discussed in this paper (a) and a three-dimensional (3-D) map of the E271 sample location near the EPR at 13°N (b).

to the west (Choukroune et al., 1984); the western side has a series of small horsts and grabens that run parallel its axis, while earlier tectonic features are obliterated on the eastern flank by two seamounts (Hekinian et al., 1983a). The crest of the ridge has a strike of 345° north while its axial zone is about 1 500 m wide (Hekinian et al., 1983b); the summit of this ridge contains an axial graben that averages 200–600 m in width and 20–50 m in depth (Ballard et al., 1984; Hekinian and Fouquet, 1985; Fouquet et al., 1988), while water depth at the graben floor varies ca. 2 700–2 500 m (Hekinian et al., 1983b). This axial graben is mostly composed of basalt and is covered with a small amount of sediment (Ballard et al., 1984), while most measured hydrothermal activity is concentrated along a 20 km stretch that parallels the strike of the central graben (Lalou et al., 1985). Two small and overlapping spreading centers are also present along the ridge segment where the axis exhibits two en echelon spreading segments, at 12°37′N and at 12°54′N (Crane, 1987; Antrim et al., 1988; Charlou et al., 1991).

A field of metalliferous sediments encompassing an area of ~200×10^3 km^2 was discovered in the EPR 9°–14°N. This field of metalliferous sediments is asymmetric, with an eastern boundary that is 300 km and a western boundary that is 200 km from the EPR axis, respectively (Gurvich, 2006).

3 Material and analytical methods

The sediment core E271 (12°39′52″N, 104°08′12″W) analyzed in this paper was collected near the EPR at 13°N using a box corer during the DY105–14 cruise (on board the R/V *Dayang Yihao* in November, 2003), from a water depth of 3 085 m, about 25 km to the west of the rise axis (Fig. 1).

The core E271 is 43 cm long and comprises three obviously different colored layers, deep reddish brown from the top to a depth of 7 cm, changing gradually from brown to yellowish-green between 7 and 22 cm, and becoming greyish-green from 22 cm depth to the bottom. In order to extract enough clay minerals for analysis, the sediment core was separated into 15 samples on the basis of these different colors. All samples are placed in deionized Milli-Q (18.2 MΩ) water and desalinated by surging with ultrasonic waves.

Major elements of the bulk sediment were analyzed using an inductively coupled-atomic emission spectrometry (ICP-AES) at the Qingdao Institute of Marine Geology; while trace elements were analyzed using inductively coupled plasma-mass spectrometry (ICP-MS) (ELAN DRC II) at the Institute of Oceanology, Chinese Academy of Sciences (IOCAS). Total dissolution of the samples was performed by HNO_3–HF/$HClO_4$ high pressure decomposition in a Teflon vial (Wang et al., 2014). The dissolved samples were subjected to ICP-MS with relative standard deviation (RSD) set to less than 3%. They were then immediately analyzed for Ti, Al, Fe and Mn using ICP-AES with RSD set to less than 2%. The precision of ICP-MS and ICP-AES analyses was checked via comparisons with national marine sediment level standard substances GBW07315 and GBW07316 as well as the United States Geological Survey basalt standards BCR-2 and BHVO-2.

In order to get the clay minerals in each sediment samples, a series of chemical procedures were carried out. Organic matter, carbonate, biogenic opal, amorphous and poorly crystalized Fe-Mn oxides were carefully removed using washes of 10% H_2O_2 at 60°C for 1 h (Huang et al., 2016), 10% acetic acid (HOAc) at 60°C for 1 h, 1 mol/L NaOH at 80°C for 1.5 h (Wan et al., 2007, 2010), 1 mol/L NH_2OH·HCl in 25% (v/v) HOAc at 80°C for 1.5 h (Chester and Hughes, 1967; Dunk and Mills, 2006; Yu et al., 2012), respectively. The solid sample for each procedure was then centrifuged twice with deionized Milli-Q water with the exception of the last one, which was centrifuged three times. Subsequent mineralogical and geochemical studies were carried out on clay minerals (<2 μm), separated using the conventional Stokes' settling velocity principle.

Clay minerals were identified via XRD using a D8 ADVANCE diffractometer with CuKα radiation (40 kV and 40 mA) at the IOCAS. The determinations were carried out four times: (1) on air-dry samples (3°–30° 2θ, at 0.02° steps), (2) on glycolated samples (3°–30° 2θ, at 0.02° steps), and (3) on glycolated samples (24°–26° 2θ, at 0.01° steps), (4) on randomly oriented powders of samples (3°–60° 2θ, at 0.02° steps). Glycolated clay was pretreated with an ethylene-glycol solution at 60°C for 12 h. Relative percentages of the four main clay mineral groups, smectite (including mixed-layers) (15–17 Å), illite (10Å), and kaolinite/chlorite (7 Å) were estimated by weighting the peak areas of the basal reflection of glycolated samples using the software Topas 2P and the empirical factors outlined by Biscaye (1965).

Major elements of clay minerals were analyzed using X-ray fluorescence (XRF) spectrometry (ARL9800XP+) at the Center of Modern Analysis, Nanjing University, while loss on ignition (LOI) was measured after 10 h of calcination at 960°C. Next, 0.6 g of each sample was mixed with dilithium tetraborate ($Li_2B_4O_7$: $LiBO_2$ = 67:33) flux (flux:sample=11:1) in a Pt-Au crucible, fused with LiBr (40 mg/mL, 0.6 ml) in a muffle oven to generate a fusion sample disc, and then measured with a XRF. Contents of major elements were analyzed by comparison with standard samples and control experiments; analytical uncertainties were 0.5% for SiO_2 and 0.2% for Al_2O_3, while the relative error for CaO, K_2O, Fe_2O_3, and TiO_2 were less than 5% and less than 10% for MgO, Na_2O, P_2O_5, and MnO. Total iron is expressed as Fe_2O_3, and trace elements of clay minerals were analyzed using ICP-MS at the IOCAS, following the same analytical method as that described above for the bulk sediments.

Analysis of Si isotopes in clay minerals was carried out using the SiF_4 method for δ^{30}Si (Liu et al., 2013) in the Analytical Laboratory of Beijing Research Institute of Uranium Geology. All results were recorded as δ^{30}Si values against NBS-28, as follows: $\delta^{30}Si_{NBS\text{-}28}= [(^{30}Si/^{28}Si)_{Sample}/(^{30}Si/^{28}Si)_{NBS\text{-}28}-1]\times10^3$. The analytic precision of this approach was better than ± 0.1‰, determined via repeated fluorination and by comparison with two Chinese national reference materials for Si isotopes, GBW04421 and GBW04422.

An aliquot from each sample was treated to remove carbonate using 2% acetic acid (Cuadros et al., 2011). Au-coated fragments of bulk and carbonate-free sediments were used for SEM observations at the IOCAS. The SEM system we used combined a TESCAN VEGA 3 LMH SEM with an Oxford INCA X-Max energy dispersive spectrometer (EDS). Loose sediments were fixed onto SEM stubs with double glue, and were imaged using backscattered electrons. Standard analytical operating conditions included an accelerating voltage of 20 kV, a beam intensity of 15, and a working distance of ~15 mm.

4 Results

4.1 *Sediment minerals*

Previous studies on the core E271 have demonstrated that it was composed of amorphous or poorly crystalline Fe-Mn oxides, clay minerals, quartz, and feldspar, as well as a trace amount of barite, and some biogenic detritus, such as coccolith, fo-

raminifera, diatom (Yu, 2010; Wu, 2012), which is consistent with the investigation of the sediments in this area (Gurvich, 2006; Xue, 2003).

SEM studies of sediment samples from the E271 core reveal that the most abundant biogenic components are calcareous and siliceous debris (Fig. 2). Of these components, calcareous microfossils are common, comprising mainly coccoliths followed by foraminifera, both in variable stages of preservation. The siliceous biogenic debris content of samples is lower, comprised of diatoms, radiolarians, and silicoflagellates. Of these, the diatom content is highest while siliceous microfossils exhibit varying degrees of dissolution. We also observed little evidence for the presence of volcanic debris in sediments; when present, this debris shows no evidence for surface dissolution or alteration.

4.2 *Sediment geochemistry*

All sediment samples from the Core E271 are characterized by high Fe and Mn contents, 9.15–13.56 wt% and 1.60–3.31 wt%, respectively, as well as low Ti and Al contents, 0.20–0.26 wt% and 3.91–5.02 wt%, respectively. They exhibit typical characteristics of metalliferous sediments (Boström, 1973; Lisitzin et al., 1976), including Al/(Al+Fe+Mn)<0.3, Fe/(Al+Fe+Mn)>0.5, and (Fe+Mn)/Al>2.5. All sediment samples are plotted in the hydrothermal field in the Mn–Fe–(Co+Ni+Cu)×10 ternary diagram (Fig. 3).

Meanwhile the shale-normalized (Haskin and Haskin, 1966; Piper, 1974) REE distribution patterns of these elements exhibit obviously negative Ce anomaly (Ce / Ce* = 0.35–0.44), no Eu anomaly (Eu / Eu* = 1.04–1.13), and enrichment of heavy REE (HREE) relative to light REE (LREE) (Fig. 4). These characterist-

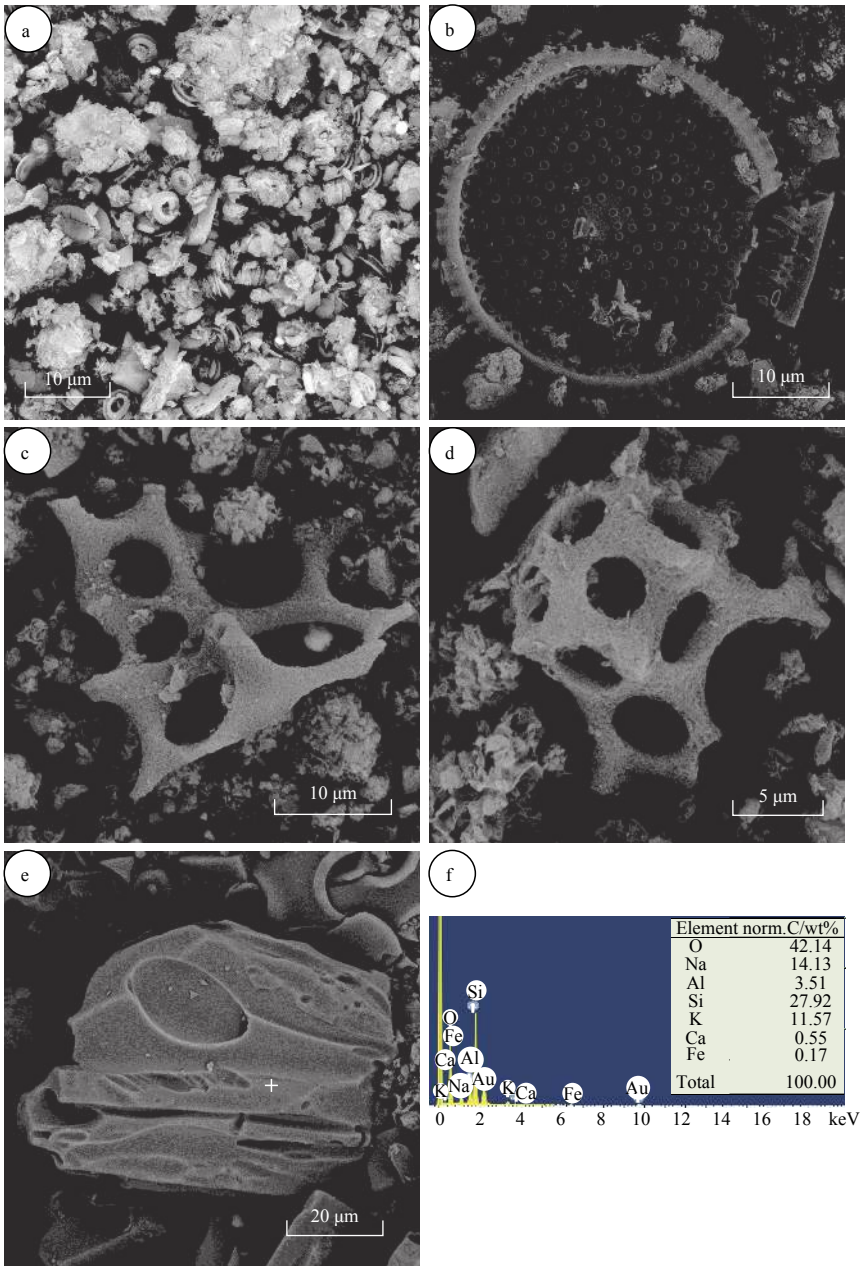

Fig. 2. SEM images of sediments and EDS spectra of selected area. a. Coccoliths and some fine-grained materials; b. a well-preserved diatom; c and d. siliceous microfossils showing strong dissolution; e. vesicular glass grain with blocky shape; f. EDS spectra of an selected area of Au-coated sample in the (e) and the spot analyzed is marked with a cross (f).

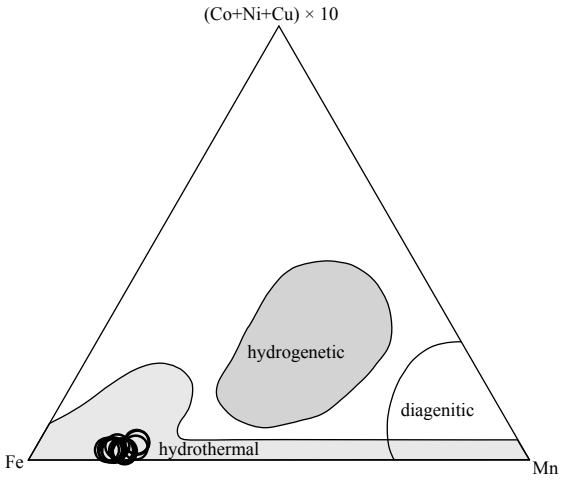

Fig. 3. Mn-Fe-(Co+Ni+Cu)×10 ternary diagram of Core E271 (after Bonatti et al., 1972). The open circles are E271 sediment samples.

ics are similar to those of pacific deep seawater, as well as metalliferous sediments from the Southeast Pacific (Fig. 4) and from the east of the EPR near 13°N (Xue, 2003). All suggest that the E271 sediments are metalliferous sediments.

The REE contents of sediments range 117×10^{-6}–202×10^{-6} (Table 1), a little lower than those of sediments from the east of the EPR near 13°N (128×10^{-6}–288×10^{-6}; Xue, 2003), that may be because of the slight lower hydrothermal Fe in this study (8.16–17.27 wt%, Xue, 2003), which scavenges REE from seawater (German et al., 1990).

4.3 *Clay minerals*

XRD determinations of all 15 clay mineral samples reveal that there are no differences in kinds of minerals of these samples, except only slight differences in mineral composition between samples from deferent depths. The contents of smectite are higher than those of other clay minerals, ranging 52.5%–75.8% (average: 68.2%; Figs 5 and 6). These proportions increase slowly in concert with depth from the top of the profile to a depth of 22 cm before varying a little from this depth to the base of the core. The contents of illite vary from 16.7% to 32.3% (average: 23.4%), while the trend in the contents of illite versus depth is opposite to that of smectite from the top of the core to a 22 cm depth, decreasing as depth increases. In addition, the contents of kaolinite are low, ranging 4.6%–17.4%, while the contents of chlorite are the lowest, usually less than 3.0%, with the exception of the top of the core. Results show that S/I (smectite/illite) ratios encompass a large range of variation, 1.64–4.53 (average: 3.07). Some quartz and feldspar are also present in clay minerals, but less than 3% and 5%, respectively.

4.4 *Clay geochemistry*

The results of this study (Table 2) show that clay minerals in sediments from the E271 core have particularly high Fe_2O_3 contents, ranging 20.31wt%–30.41wt% (average: 25.11wt%), which suggests the smectite is enriched in Fe. Although the contents of Al_2O_3 are also high, ranging 6.04wt%–12.90wt%, these clay minerals have lower TiO_2, MnO, and MgO contents, ranging 0.32wt%–0.64wt%, 0.10wt%–0.60wt% and 2.20wt%–2.82 wt%, respectively.

Our results show that the total REE and Y contents of E271 clay minerals are low, 19.04×10^{-6}–110.67×10^{-6}, much less than the values seen in terrigenous clay minerals in sediments from the Chinese ferromanganese nodule survey area, between the Clarion and Clipperton fractures (CC zone) of the eastern Pacific (200×10^{-6}–350×10^{-6}; Liu et al., 2005). The shale-normalized REE distribution patterns of clay minerals are moderately fractionated with HREE enrichment relative to LREE. These minerals also exhibit negative Ce anomaly (Fig. 4) and their Ce/Ce* values range in 0.51–0.82.

δ^{30}Si values for E271 clay minerals vary greatly between –1.1‰ and –0.4‰, within the range of weathering-related clay minerals (–2.3–+0.1‰; Douthitt, 1982; De La Rocha et al., 2000; Ziegler et al., 2005), a little negative compared with the average δ^{30}Si value of igneous materials (–0.3±0.3‰; Douthitt, 1982; Ding et al., 1996).

5 Discussions

5.1 *Clay minerals sources*

The study area is located close to the Mexican south coast, about 650 km from the city of Acapulco. As previous researchers have suggested that the detrital clay mineral assemblage seen in North Pacific marine sediments is characterized by abundant illite and chlorite derived from aeolian dust (Kadko, 1985; Chamley, 1989), it is likely that some of the clay minerals in core E271 may be derived from Mexico or Central America. Indeed, investigations of aeolian dust collected off the southwest coast of southern Mexico and Guatemala, in samples L66K4 and L66K5, respectively, demonstrate the predominance of illite, kaolinite, and chlorite in clay minerals, with just a small smectite component (<1%; Leinen et al., 1994; Fig. 7). Thus, most of the illite, kaolinite, and chlorite in the core E271 sediments likely originates from Mexico or Central America transported by winds (Hovan, 1995). Clay mineral composition of the L66K4 and L66K5 aeolian dust is similar to sediments from the southern Mexican margin (Fig. 7), which also suggests that a component of the clay minerals studied, with the exception of smectite, may be derived from Mexican rivers (McMillen et al., 1982).

The smectite/illite (S/I) ratio of clay minerals can reflect the relative contributions of the authigenic and terrigenous clay minerals (Liu et al., 2005 and references therein); a higher ratio indicates increased authigenic smectite content. The mean S/I ratio in South Pacific sediments is 2.04 (Chamley, 1989), higher than that in North Pacific sediments (0.85; Chamley, 1989); although the study area discussed here is located in the North Pacific, the S/I ratios (1.64–4.53; n=15) in E271 sediments are even higher than that in the South Pacific sediments with the exception of the top two samples. This also implies that abundant authigenic smectite is present in E271 metalliferous sediments.

5.2 *Smectite formation mechanism*

In addition to a detrital source, the bulk of smectite is authigenic in ocean sediments. Four general mechanisms have been proposed for the formation of authigenic smectite in the deep ocean.

Firstly, authigenic smectites can be formed via the alteration of volcanic rock fragments and glass in the marine environment (Hein and Scholl, 1978; Cole and Shaw, 1983). Indeed, smectite minerals are widespread in basal marine deposits, deep-sea ash beds, and groundmass veins (Banks, 1972; Melson and Thompson, 1973; Scheidegger and Stakes, 1977; Hein and Scholl, 1978; Seyfried et al., 1978; Lackschewitz et al., 2006). In addition, in places where a high content of volcanic authigenic smectite

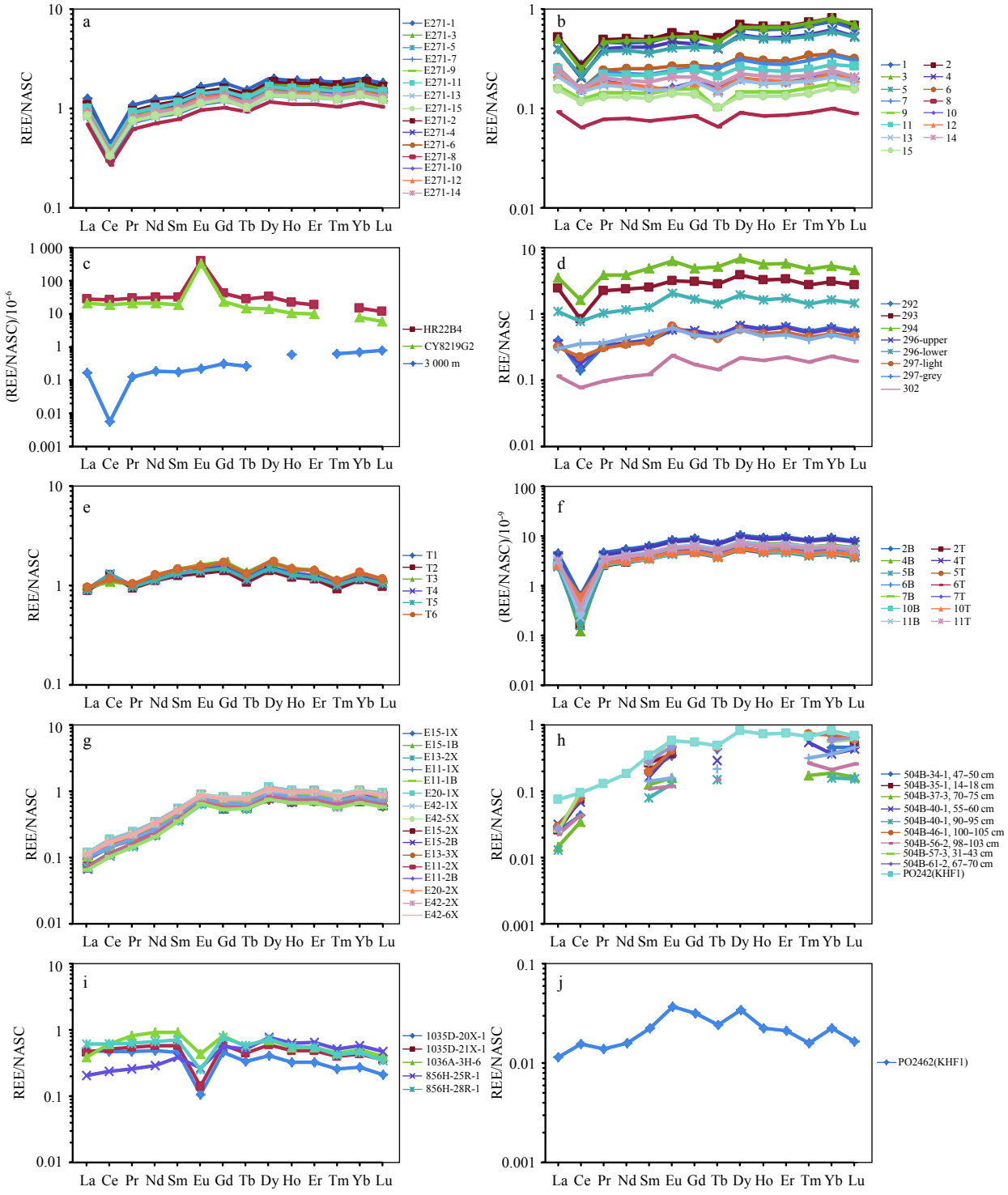

Fig. 4. Plots of shale-normalized REE (Haskin and Haskin, 1966; Piper, 1974) distribution patterns. a. E271 sediments; b. E271 clay minerals; c. hydrothermal fluids from the EPR at 13°N (the upper two samples, Douville et al., 1999) and deep (3 000 m) seawater from the eastern Pacific (the lower sample, De Baar et al., 1985); d. metalliferous sediments from the Southeast Pacific (Dekov et al., 2010); e. terrigenous clay minerals from the Chinese ferromanganese nodule survey area, eastern Pacific (Liu et al., 2005); f. distal hydrothermal plume particles (<0.3–1 km from the vent site) collected from the EPR at 9°45′N (Sherrell et al., 1999); g. basalts from near EPR 13°N (Zhang et al., 2008); h. clay minerals formed by the alteration of basalt from the Kolbeinsey hydrothermal field off the north coast of Iceland (Lackschewitz et al., 2006) as well as from Hole 504B, Leg 70, Costa Rica Rift (Sharaskin et al., 1983); i. clay minerals formed by the hydrothermal alteration of sediments from the Bent Hill massive sulfide and active venting area on the Juan de Fuca Ridge (Lackschewitz et al., 2000); j. clay minerals precipitated within active chimneys from the PO 246A-1 core, Grimsey hydrothermal field, north coast of Iceland (Lackschewitz et al., 2006).

Table 1. Major elements (in wt%) and trace elements (10^{-6}) of E271 core sediment samples from near EPR at 13°N

Sample No.	1	2	3	3[a]	4	5	6	7	8	9	10	11	12	13	13[a]	14	15
Cored Interval Below Sea Floor/cm	0-2	2-4	4-7	4-7	7-10	10-13	13-16	16-19	19-22	22-25	25-28	28-31	31-34	34-37	34-37	37-40	41-43
wt%																	
Ti	0.26	0.26	0.26	0.25	0.25	0.23	0.23	0.23	0.23	0.23	0.23	0.22	0.21	0.22	0.20	0.20	0.20
Al	5.02	4.95	4.84	4.78	4.75	4.84	4.46	4.46	4.49	4.44	4.36	4.33	4.12	4.11	4.03	3.91	3.95
Fe	12.74	12.65	12.76	12.8	12.60	12.63	13.56	13.55	13.22	12.46	12.15	10.93	10.76	9.12	9.18	9.51	10.18
Mn	3.26	3.28	3.30	3.32	2.84	2.88	3.11	3.02	2.86	2.50	2.33	2.00	1.99	1.68	1.52	1.77	2.00
Ca	2.68	2.76	2.88	2.96	3.16	3.08	3.48	3.52	4.60	6.12	8.32	10.16	8.12	7.41	7.47	5.12	3.20
Al/(Al+Fe+Mn)	0.24	0.24	0.23	0.23	0.24	0.24	0.21	0.21	0.22	0.23	0.23	0.25	0.24	0.28	0.27	0.26	0.24
10^{-6}																	
Co	40.8	39.0	28.5	27.7	25.3	22.5	21.3	19.9	20.9	18.2	26.5	30.7	25.3	22.8	21.0	24.5	22.6
Ni	199	165	152	142	142	132	124	124	135	109	125	125	107	103	91	105	110
Cu	454	460	306	292	152	183	153	221	210	358	213	167	151	144	126	132	130
La	51.5	44.9	40.6	41.8	38.6	37.5	35.6	33.9	28.5	36.5	41.7	41.4	33.8	35.6	36.4	34.6	
Ce	36.4	29.5	26.5	27.3	26.6	26.2	25.6	25.1	22.7	29.1	32.8	32.5	30.2	27.9	29.7	29.6	27.8
Pr	10.9	9.55	8.75	8.77	8.28	8.18	7.69	7.29	6.32	8.22	9.24	9.15	8.17	7.65	7.53	8.05	7.59
Nd	47.2	41.3	38.6	37.2	35.6	35.6	33.3	31.7	27.0	35.4	39.9	39.3	34.8	33.1	31.3	34.4	32.4
Sm	9.93	9.03	8.32	8.12	7.82	7.62	7.14	6.73	5.82	7.55	8.51	8.64	7.59	7.15	7.03	7.41	6.97
Eu	2.67	2.37	2.31	2.15	2.14	2.13	1.91	1.77	1.54	1.96	2.25	2.27	2.06	1.96	1.80	1.95	1.83
Gd	11.5	10.1	9.44	9.34	8.77	8.38	8.00	7.65	6.49	8.46	9.48	9.56	8.60	7.96	7.78	8.33	7.82
Tb	1.88	1.72	1.64	1.58	1.47	1.43	1.36	1.30	1.15	1.39	1.56	1.57	1.37	1.30	1.20	1.35	1.27
Dy	11.0	10.1	9.34	9.4	8.69	8.47	8.10	7.57	6.41	8.14	9.11	9.18	8.09	7.51	7.33	8.00	7.52
Ho	2.58	2.42	2.21	2.27	2.11	2.05	1.90	1.78	1.49	1.93	2.15	2.15	1.93	1.69	1.81	1.87	1.79
Er	7.06	6.65	6.19	6.01	5.72	5.56	5.23	4.94	4.11	5.29	5.78	5.89	5.25	4.95	4.79	5.10	4.94
Tm	1.16	1.09	0.992	1.024	0.958	0.919	0.870	0.808	0.662	0.844	0.931	0.954	0.830	0.772	0.796	0.838	0.776
Yb	7.08	6.55	6.29	6.07	5.80	5.65	5.30	4.88	4.06	5.19	5.77	5.77	5.18	4.96	4.78	5.12	4.82
Lu	1.11	1.02	1.01	0.89	0.899	0.864	0.832	0.783	0.630	0.798	0.906	0.904	0.805	0.763	0.745	0.787	0.748
Y	72.6	68.9	66.1	64.7	61.3	59.8	57.2	53.4	45.1	58.1	64.6	65.4	57.3	54.9	52.1	57.1	53.0
ΣREE	202.0	176.3	162.2	161.9	153.6	150.5	142.9	136.2	116.9	150.8	170.0	169.2	152.3	141.5	142.2	149.2	140.8
Ce/Ce*	0.36	0.33	0.34	0.35	0.35	0.35	0.36	0.37	0.40	0.40	0.39	0.39	0.41	0.43	0.29	0.41	0.40
Eu/Eu*	0.76	0.76	1.11	1.05	0.79	0.81	0.77	0.75	0.76	0.75	0.76	0.76	0.78	1.10	1.00	0.75	0.75

Note: $Ce/Ce^* = 2Ce_N/(La_N+Pr_N)$; $Eu/Eu^* = 2Eu_N/(Sm_N+Gd_N)$; subscript N means normalization by the value of North American Shale Composite (NASC) (Haskin and Haskin, 1966; Piper, 1974); subscript a indicates the analysis result of a parallel sample.

has been formed in marine sediments, zeolites (phyllipsite and clinoptilolite) and/or calcitic plagioclase, pyroxenes and volcanic glass are all found associated with authigenic smectite (Griffin et al., 1968). The combined formation reaction for this process is as follows:

Basalt + K^+ + Na^+ + SiO_2 + H_2O + H^+ → phillipsite + smectite + Ca^{2+} + Fe_2O_3 (Piper and Heath, 1989)

Although clay minerals that are derived from the alteration of volcanic debris, including the <10 μm fraction in sediments from the EPR at 9°N near the Siqueiros fracture zone (Rateev et al., 1980), have similar clay mineral contents to E271 samples in the Al_2O_3-Fe_2O_3-MgO plot (Fig. 8), additional evidence suggests that these clay minerals are not products of volcanic alteration.

Volcanism is active in both axial and off-axial areas along the EPR at 13°N (Hekinian and Fouquet, 1985), but only traces of volcanic debris are found in E271 metalliferous sediments. Indeed, SEM investigation of sediments shows that there is no textural evidence for the presence of authigenic smectite on volcanic debris, with only slight or no erosion to surfaces. In addition, previous studies (Wu, 2012) and XRD of clay minerals highlights the absence of zeolites; these findings imply that the smectite in E271 metalliferous sediments may be not derived from the alteration of volcanic debris.

In the axial area hydrothermal fields of the EPR at 13°N, smectite can be formed beneath the seafloor by the alteration of basalt and hydrothermal fluids; in this process, smectite particles detach from the basalts and travel within the hydrothermal plume to be deposited later in metalliferous sediments. But Cuadros et al. (2011) considered that, in such a setting, these diffuse hydrothermal fluids may be unable to detach and carry clay particles away.

The REE distribution patterns of clay minerals formed by the alteration of basaltic rocks are generally similar to those of host basalts (Sharaskin et al., 1983). Indeed, shale-normalized REE distribution patterns of basalts from near EPR 13°N are characterized by much more enrichment with HREE compared to E271 clay minerals and terrigenous clay minerals from eastern Pacific (Fig. 4) and have no Ce anomaly. These characteristics are also seen in clay minerals formed by the alteration of basalt and glass (Sharaskin et al., 1983; Lackschewitz et al., 2006; Fig. 4); these examples are very different from E271 clay minerals, suggesting that authigenic smectites in E271 sediments are not formed by alteration of basalt fragments and glass.

Secondly, authigenic smectites can be formed by hydro-

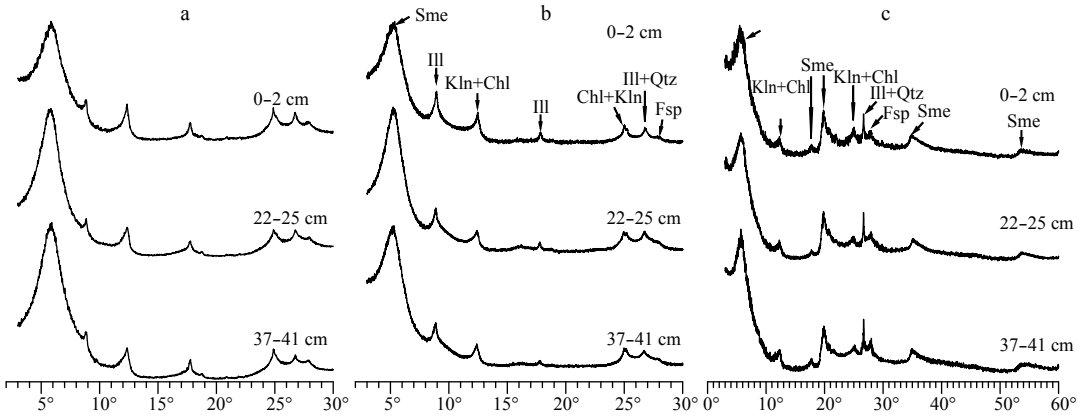

Fig. 5. XRD patterns of the clay minerals. a. Air-dried mounts of samples; b. glycolated mounts of samples; and c. randomly oriented powders of samples. Sme represents smectite; Kln, kaolinite; Ill, illite; Chl, chlorite; Qtz, quartz; and Fsp, feldspar.

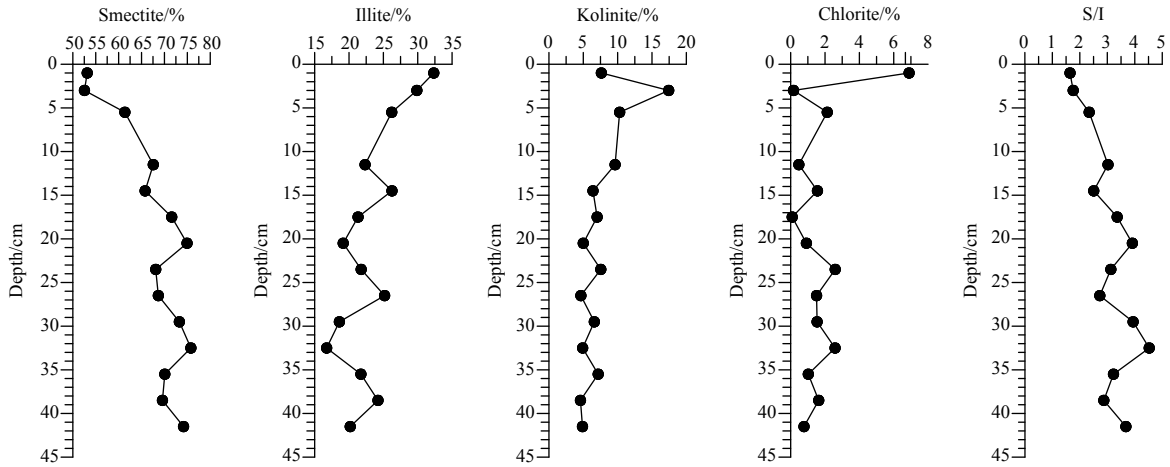

Fig. 6. Plots of mineral composition and S/I ratios of clay minerals from Core E271 samples.

thermal alteration of sediments. Within hydrothermal fields, high fluxes of hot fluids invade overlying clastic sediments and cause metasomatic reactions, such as smectite, chlorite, and talc alteration (Zierenberg and Shanks, 1994). Commonly encountered alteration products include chlorite, mixed-layer chlorite/smectite, Mg-smectite, Mg-Fe smectite, and talc (Buatier et al., 1994; Zierenberg and Shanks, 1994; Lackschewitz et al., 2000). These products are characteristic to the sediment-covered hydrothermal fields, including the Middle Valley of the JdFR (Lackschewitz et al., 2000; Dekov et al., 2008), the Escanaba Trough of the Gorda Ridge (Zierenberg and Shanks III, 1994; Dekov et al., 2008), the east flank of the JdFR revealed by Ocean Drilling Program (ODP) Leg 168 (Buatier et al., 2001; Buatier et al., 2002), the Kick'em Jenny Hydrothermal field off the northern coast of Grenada in the Lesser Antilles subduction zone (Carey et al., 2016), and the Ashadze-1 hydrothermal field in the Mid-Atlantic Ridge 13°N (Gablina et al., 2014). These altered clay minerals are often rich in MgO (3.94wt%–30.10wt%, Buatier et al., 1994; 3.79wt%–9.01wt%, Zierenberg and Shanks, 1994; 11.45wt%–30.96wt%, Lackschewitz et al., 2000; and 23.79wt%, Dekov et al., 2008), but MgO contents in the study clay minerals are lower than those of altered clay minerals, only range from 2.20wt% to 2.82wt%. Meanwhile clay minerals of alteration of sediments also show different from the study clay minerals in Fe_2O_3 and Al_2O_3 contents (Fig. 8). The shale-normalized REE patterns of hydrothermally altered clay minerals show obviously negative Eu anomaly, which are also different from those of E271 clay minerals (Lackschewitz et al., 2000; Fig. 4).

Thirdly, smectites can precipitate directly from hydrothermal fluids as the result of mixing with seawater during marine hydrothermal activity. One example of this process is smectite in the Red Sea metalliferous sediments (Bischoff, 1972); however, these Red Sea clay minerals are rich in Fe and low in Al and Mg (Fig. 8), obviously different from E271 clay minerals. Authigenic smectite that is the result of hydrothermal fluid precipitation is also observed in other fields, including in the active Grimsey hydrothermal field off the north coast of Iceland (Lackschewitz et al., 2006), in the Explorer Ridge (Grill et al., 1981), in the Area of Active Venting (AAV) as well as at the Bent Hill (Percival and Ames, 1993) and in the Cobb offset of the JdFR (Murnane and Clague, 1983), in the Escanaba Trough of the Gorda Ridge (Zierenberg and Shanks III, 1994), in the southern trough of the Guaymas Basin in the Gulf of California (Peter and Scott, 1988), and at the Red Seamount on the EPR at 21°N (Alt et al., 1987; Alt, 1988). These smectites are located near vents or in/on chimneys and mounds, but are not present in the metalliferous sediments that are far away from hydrothermal vents. Indeed, Lackschewitz et al. (2006) proposed that Mg-rich smectite can be directly precipitated as a result of interactions between hydrothermal fluids and cold Mg-rich seawater in the mixing zone at temperatures

Table 2. Major elements (wt%), REE ($\times10^{-6}$) and δ^{30}Si (‰) values of clay minerals from core E271 sediments

Sample No.	S1	S2	S3	S3[a]	S4	S5	S6	S7	S8	S9	S10	S11	S12	S13	S13[a]	S14	S15
Cored Interval Below Sea Floor/cm	0–2	2–4	4–7	4–7	7–10	10–13	13–16	16–19	19–22	22–25	25–28	28–31	31–34	34–37	34–37	37–40	40–43
wt%																	
SiO_2	40.86	39.84	39.64	38.26	39.98	40.50	42.63	43.56	47.83	49.20	49.32	48.10	49.04	48.56	49.6	49.32	48.17
TiO_2	0.64	0.60	0.59	0.53	0.45	0.51	0.49	0.47	0.32	0.54	0.62	0.62	0.64	0.62	0.58	0.61	0.57
Al_2O_3	11.72	11.06	10.9	9.3	8.44	9.28	9.04	8.67	6.04	11.11	12.30	12.58	12.90	12.42	12.32	12.08	11.05
$Fe_2O_3^T$	26.50	27.99	30.4	30.28	30.07	30.41	27.82	28.55	28.55	21.41	20.46	20.66	20.31	21.01	20.03	20.77	22.32
MnO	0.42	0.50	0.58	0.62	0.60	0.50	0.40	0.31	0.10	0.09	0.07	0.07	0.07	0.07	0.05	0.07	0.08
CaO	2.02	2.02	1.89	1.97	2.74	1.87	2.56	2.03	2.48	2.43	2.14	2.58	2.13	2.09	1.97	2.08	2.02
Na_2O	0.30	0.27	0.27	0.23	0.19	0.24	0.21	0.16	0.15	0.23	0.30	0.27	0.33	0.29	0.25	0.31	0.25
K_2O	1.26	1.18	1.15	1.11	1.12	1.25	1.34	1.41	1.62	1.65	1.59	1.45	1.62	1.51	1.61	1.62	1.53
MgO	2.26	2.21	2.23	2.17	2.31	2.25	2.45	2.38	2.66	2.80	2.78	2.82	2.75	2.81	2.61	2.76	2.73
P_2O_5	3.68	4.02	3.71	4.01	3.85	3.36	3.15	2.96	1.36	1.02	1.30	1.15	1.02	1.68	1.62	1.17	1.80
LOI	10.04	10.05	9.31	9.26	9.53	9.58	9.89	8.57	9.41	9.39	9.16	8.61	8.98	9.51	9.71	8.85	9.65
TOTAL	99.70	99.73	100.67	97.74	99.28	99.75	99.98	99.07	100.51	99.88	100.05	98.93	99.81	100.57	98.35	99.65	100.17
10^{-6}																	
La	21.00	21.48	20.6	20.34	16.40	15.95	10.45	10.38	3.83	6.98	9.59	10.42	9.25	8.8	8.7	10.13	6.35
Ce	22.89	22.00	20.71	20.51	17.03	17.53	12.89	12.60	5.40	10.20	12.98	13.06	13.15	12.25	12.11	13.09	9.71
Pr	4.75	4.95	4.81	4.71	4.00	3.83	2.46	2.38	0.79	1.45	1.92	2.24	1.84	1.77	1.73	2.06	1.32
Nd	17.27	19.03	18.48	18.16	15.77	14.74	9.62	8.57	3.01	5.49	6.60	8.19	6.66	6.45	6.15	7.27	5.02
Sm	3.51	3.73	3.6	3.66	3.11	2.75	1.90	1.66	0.57	1.06	1.17	1.63	1.25	1.15	1.13	1.39	0.95
Eu	0.86	0.93	0.89	0.81	0.76	0.66	0.43	0.39	0.13	0.25	0.26	0.38	0.25	0.24	0.26	0.33	0.23
Gd	3.31	3.44	3.32	3.44	2.87	2.62	1.72	1.62	0.54	1.00	1.17	1.58	1.18	1.18	1.22	1.33	0.89
Tb	0.59	0.64	0.6	0.54	0.49	0.50	0.32	0.32	0.08	0.12	0.20	0.26	0.19	0.17	0.19	0.21	0.13
Dy	3.56	3.87	3.73	3.51	3.07	2.96	1.81	1.72	0.50	0.81	1.10	1.44	1.12	1.09	1.03	1.24	0.74
Ho	0.83	0.90	0.89	0.87	0.69	0.67	0.41	0.38	0.11	0.20	0.26	0.33	0.26	0.27	0.21	0.28	0.18
Er	2.36	2.54	2.52	2.46	1.96	1.90	1.13	1.05	0.32	0.55	0.70	0.89	0.71	0.71	0.65	0.79	0.50
Tm	0.43	0.47	0.46	0.46	0.35	0.34	0.22	0.19	0.06	0.10	0.13	0.16	0.12	0.13	0.11	0.14	0.09
Yb	2.64	2.86	2.89	2.85	2.19	2.13	1.25	1.21	0.36	0.63	0.80	0.97	0.79	0.77	0.71	0.86	0.58
Lu	0.39	0.42	0.43	0.41	0.33	0.32	0.19	0.19	0.05	0.10	0.12	0.16	0.12	0.09	0.13	0.13	0.10
Y	18.79	20.33	20.42	20.24	14.86	14.75	8.83	9.21	2.96	5.13	7.01	8.69	6.90	6.42	6.68	8.02	4.72
ΣREE	84.37	87.25	83.93	82.71	69.03	66.89	44.81	42.65	15.76	28.95	37.00	41.71	36.90	35.07	34.33	39.23	26.76
Ce/Ce*	0.56	0.52	0.51	0.51	0.52	0.55	0.62	0.62	0.76	0.78	0.74	0.66	0.78	0.76	0.76	0.70	0.82
Eu/Eu*	1.08	1.11	1.10	0.98	1.08	1.05	1.01	1.02	1.00	1.04	0.95	1.00	0.88	0.88	0.94	1.06	1.07
δ^{30}Si/‰	–1.1	–0.8	–0.6		–0.6	–1.1	–0.8	–0.8	–0.8	–1	–0.4	–0.6	–0.6	–0.7		–0.4	–0.5

Note: $Fe_2O_3^T$ refers to total Fe. Superscript a indicates the analysis result of a parallel sample.

between 130°C and 250°C, and Cuadros et al. (2011) inferred that black smokers (300°C–350°C) facilitate the formation of beidellite, talc, and talc-smectite (or kerolite-smectite) rather than nontronite or saponite, while white smokers (<100°C–300°C) may produce nontronite, but the cooler temperature and slower flow velocity give white-smoker fluids less buoyancy and fewer opportunities to travel far from the vent point.

The REE distribution pattern of clay minerals precipitated within active chimneys in the Grimsey hydrothermal fields off the north coast of Iceland shows an obviously positive Eu anomaly, distinct from E271 clay minerals but similar to hydrothermal fluids (Fig. 4). Thus, one can conclude that the smectite in this study is not directly precipitated from hydrothermal fluids.

Fourthly, authigenic smectite may form in the marine environment as the result of reactions between hydrothermally-derived Fe-oxyhydroxide and biogenic silica in metalliferous sediments. This process can be seen, for example, in the Bauer Deep (Heath and Dymond, 1977; Lyle et al., 1977; Dymond and Eklund, 1978), in the manganese nodule belt of the North Equatorial Pacific (Hein et al., 1979), as well as in the Southeast Pacific (Heath and Dymond, 1977). Using transmission electron microscopy, Hoffert et al. (1981) observed the direct authigenesis of smectites on dissolving siliceous organisms, while Cole (1985) used SEM to visualize siliceous microfossil corrosion and infilling by smectite in buried sediments. While these observations confirm the Fe-oxyhydroxide and biogenic silica reaction hypothesis, Cuadros et al. (2011) also suggested that both detrital phases and X-ray amorphous silica of hydrothermal origin can provide Si for the formation of smectite.

The mineral and chemical compositions of E271 clays are very similar to those of Southeast Pacific clay minerals (Cuadros et al., 2011; McMurtry and Yeh, 1981), and to DOMES clay minerals (Hein et al., 1979; Figs 6 and 7) which also show distinctive negative Ce anomaly. These similarities suggest that all share the same origin.

In conclusion, one can conclude that the authigenic smectites in E271 clay minerals were formed by reactions between hydrothermal Fe-oxyhydroxide, silica, and seawater in metalliferous sediments.

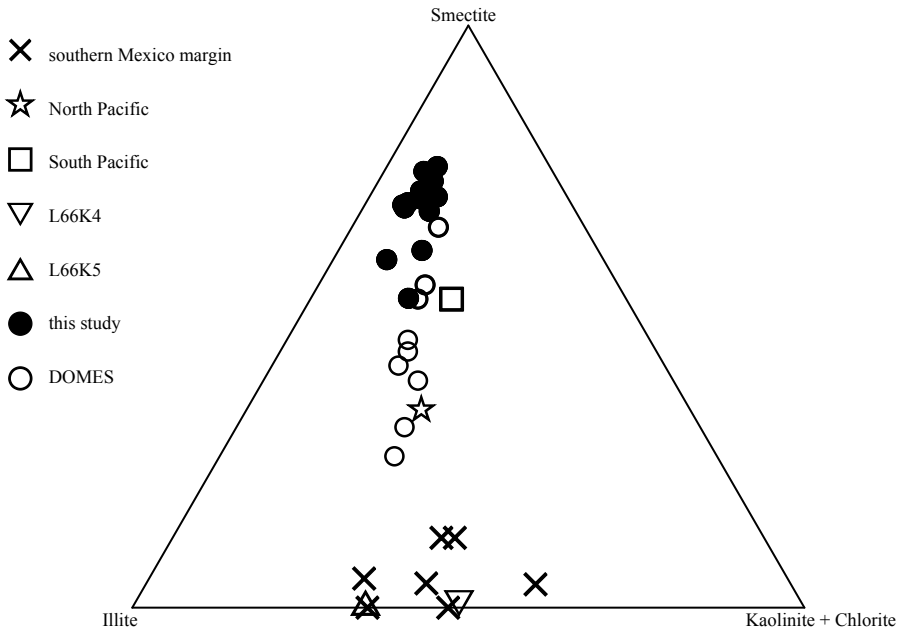

Fig. 7. The clay mineral composition of marine sediments and aeolian dust. ●, clay minerals from this study; ○, <1 μm fraction of sediments from the manganese nodule belt of the North Equatorial Pacific (DOMES) (Hein et al., 1979); ☆, North Pacific clay minerals (Chamley, 1989); □, South Pacific clay minerals (Chamley, 1989); ▽, clay minerals from aeolian dust along the southern Mexican Margin (L66K4) (Leinen et al., 1994); △, clay minerals from aeolian dust along the southern Guatemala Margin (L66K5) (Leinen et al., 1994); ×, clay minerals from the southern Mexican Margin (Schumann and Nagel, 1982).

5.3 *Geochemical behavior of silicon isotope*

Researchers have proposed a number of Si sources for authigenic smectite, including biogenic (Dymond and Eklund, 1978; Hein et al., 1979; Hoffert et al., 1981; Cole, 1985), hydrothermal (Cole and Shaw, 1983; Cole, 1985; Gurvich, 2006; Cuadros et al., 2011), and detrital sources (Cuadros et al., 2011). In this study, we try to decide the source of Si and to trace the geochemical behavior of silicon isotopes during the smectite formation.

While the compositions of E271 clay minerals are complex, Si isotope values do reflect the mean values of different minerals. Smectite contents, for example, are the highest, falling in the range of 52.5%–75.8%, followed by illite, which falls in the range of 16.7%–32.3%. Illite also has a δ^{30}Si value of –0.9‰ (Douthitt, 1982) within the range of the studied clay minerals. While the proportion of Si isotopes is much lighter in kaolinite (–2.2‰, Ziegler et al., 2005; Opfergelt et al., 2010) with an average δ^{30}Si value of (–1.6 ± 0.5)‰ (De La Rocha et al., 2000), kaolinite contents are low in the E271 clay minerals, at an average of 7.4%. Compared to the levels of detrital quartz in sediments, which range between –1.1‰ and +0.7‰ (Basile-Doelsch et al., 2005), the δ^{30}Si values of E271 clay minerals are similar, or slightly depressed. These values are also lower than those seen in detrital feldspars from the aeolian Navajo Sandstone at Black Mesa, Arizona, USA, which have a mean δ^{30}Si of (–0.15 ± 0.04)‰ (Georg et al., 2009), but both the quartz and feldspar contents in the clay fraction of E271 sediments are low (less than 3% and 5%, respectively). Through the above analysis, the δ^{30}Si values of E271 clay minerals reflect those of authigenic smectite.

The biogenic siliceous debris in marine sediments includes mainly diatoms, radiolarians, and sponge spicules, and their δ^{30}Si values range greatly (Douthitt, 1982; Fig. 9). This is because different species have particular Si isotope compositions; of these, the biogenic silica of diatoms is best documented and δ^{30}Si is known to fall in the range between –0.3‰ and + 2.6‰ (De La Rocha et al., 1998; Varela et al., 2004). Data on the δ^{30}Si values from diatoms in marine sediments from ODP Core 1 240 on the eastern equatorial Pacific range between +0.74‰ and +1.41‰ (Pichevin et al., 2009), while those of radiolarians in marine sediments from the CC zone of the Pacific Ocean exhibit values ranging between +0.2‰ and +1.2‰ (Wu et al., 1997). Although these values are all higher than those seen in E271 clay minerals, sponge spicules exhibit a wide range of much lower δ^{30}Si values between –3.4‰ and –0.9‰ (Douthitt, 1982).

Diatoms are by far the most important Si sink in the oceans (Basile-Doelsch 2006). Cole (1985) observed visually authigenic smectites as growths on microfossil surfaces and interior infillings using SEM and suggested that the smectite formation is predominantly the result of the contact reaction between Fe-oxyhydroxide and the siliceous tests of diatoms, including a silica-dissolution stage. Although the δ^{30}Si values of diatoms are higher than those of E271 clay minerals, studies have demonstrated that Si isotope fractionation occurs during the dissolution of diatom silica and results in the release of dissolved Si that is consistently about 0.55‰ lighter in δ^{30}Si than its parent SiO_2. At the same time, experiments have shown that Si isotope fractionation also takes place via the preferential adsorption of dissolved light Si isotopes by Fe-oxyhydroxide (Demarest et al., 2009; Opfergelt et al., 2009). Thus, data show that the combination of Fe-oxyhydroxide and diatom Si can produce smectite with a lighter Si isotope. Radiolarians are also important to this reaction, while the δ^{30}Si value of sponge spicules are too low, even after double Si isotope fractionations, to form smectite with a higher Si isotope ratio. We observed most of diatoms and radiolarians show dissolution (Fig. 2), which suggests that they may be a potential Si source.

The existence of hydrothermal origin Si in intimate contact

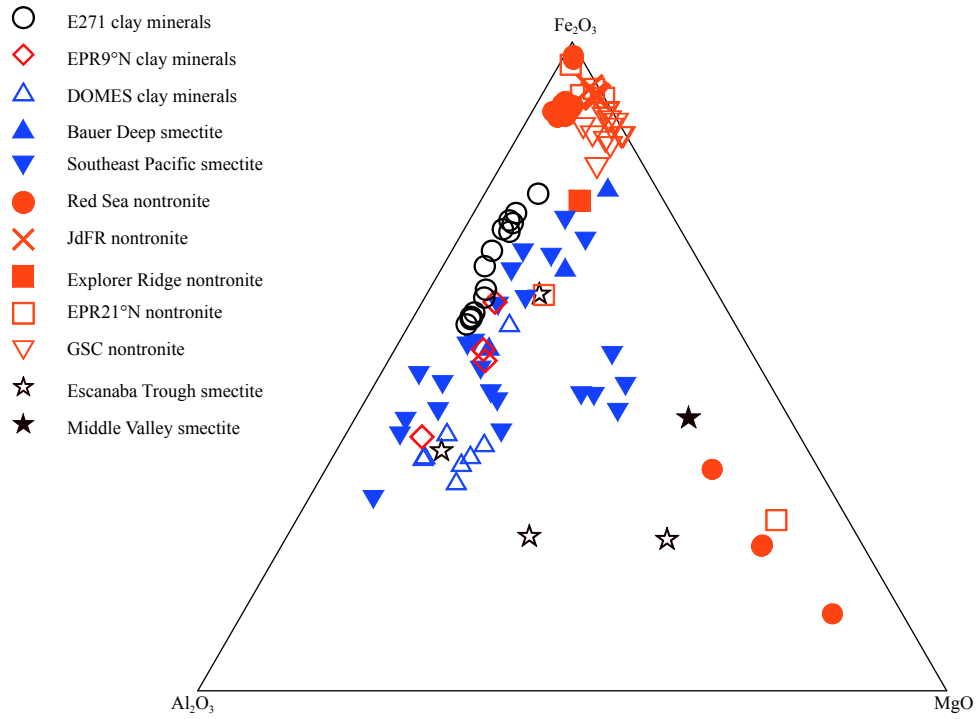

Fig. 8. An Al_2O_3-Fe_2O_3-MgO plot of clay minerals in marine sediments. ○, E271 clay minerals; ◇, <10 μm fraction in sediments from the EPR at 9°N (Rateev et al., 1980); △, <1 μm fraction in sediments from the DOMES sediments (Hein et al., 1979); ▲, Bauer Deep clay minerals including smectite granules (Dymond and Eklund, 1978), <2 μm fraction (McMurtry and Yeh, 1981) and <0.5 μm fraction (Cole, 1985); ▼, Southeast Pacific clay minerals including <2 μm fraction (McMurtry and Yeh, 1981), and smectite granules (Cuadros et al., 2011); ●, Red Sea samples including smectite granules (Bischoff, 1972), <1 μm fraction (Butuzova et al., 1979), and <0.5 μm fraction (Cole, 1988); ✕, JdFR nontronites (Murnane and Clague, 1983); ■, <2 μm fraction in hydrothermal sediments from the Explorer Ridge (Grill et al., 1981); □, nontronites from the EPR at 21°N (Hekinian et al., 1980; Alt et al., 1987; Alt, 1988); ▽, Galapagos spreading center clay minerals including <2 μm fraction (Honnorez et al., 1983), <1 μm fraction (Rateev et al., 1980), and nontronite granules (Barrett et al., 1983); ★, <2 μm fraction in sediments from the Middle Valley (Buatier et al., 1994); ☆, Escanaba Trough smectites (Zierenberg and Shanks III, 1994; Dekov et al., 2008). The red color denotes alteration products of volcanic rock fragments and glass, while blue denotes low-temperature interactions between Fe-oxyhydroxide and silica, orange denotes hydrothermal precipitates, and dark brown denotes sediment hydrothermal alteration products.

with Fe-oxide precipitates from hydrothermal fluids makes the latter a potential source of silica as the result of sediment diagenetic reactions (Cuadros et al., 2011). Although two hydrothermal fluid samples from vents on the EPR at 9°N have slightly elevated δ^{30}Si values (between –0.4‰ and –0.2‰, De La Rocha et al., 2000) compared with E271 clay minerals, Si isotope fractionation during the combination of Fe-oxyhydroxide and light Si isotopes from hydrothermal fluids lowers the δ^{30}Si values of newly formed smectite.

In earlier work, Cuadros et al. (2011) reported that detrital silicates provided Si and Al for smectite formation. Although we do not know which kinds of detrital silicates supply Si and what their δ^{30}Si values are, the continental dust of sediments from the central Pacific has a mean δ^{30}Si value of –0.5‰ (Ding et al., 1996; Ziegler et al., 2005). Indeed, Savage et al. (2013) determined that Pleistocene loess samples exhibit a narrow range of Si isotopic compositions (range between –0.28‰ and –0.15‰) and calculated that upper continental crust has a weighted average composition of δ^{30}Si of –0.25‰ ± 0.16‰ (accurate to two standard deviations), close to that of mafic and ultramafic igneous rocks (–0.3‰ ± 0.3‰, Douthitt, 1982; Ding et al., 1996). These values are all slightly higher than those of the study samples, which are therefore available for the authigenesis of smectite because of the preferential adsorption of lighter Si isotope onto Fe-oxyhydroxide during weathering of detrital silicates (Opfergelt et al., 2009).

In summary, it is not useful to determine which kinds of Si sources are more important in the smectite formation based on δ^{30}Si values, while a Si isotope fractionation occurs during the smectite formation which results in the δ^{30}Si values of newly formed smectite lower than parent SiO_2.

5.4 *REE*

In order to investigate REE behavior in both hydrothermal particulates and metalliferous sediments, we analyzed the REE/Fe (represented by Sm/Fe mass ratio) in different phases. Results show that the Sm/Fe mass ratios of proximal hydrothermal plume particles (range from <0.5 m to 20 m from the vent) on the EPR 13°N vary in 0.6×10^{-6}–3.2×10^{-6} (German et al., 2002), while those of distal hydrothermal plume particles (range from <300 m to 1 km from the vent) on the EPR 9°45′N (Sherrell et al., 1999) are higher, 2.9×10^{-5}–5.2×10^{-5}, which results from continued scavenging of REE from seawater as the plume disperses and particles age (German et al., 1990; Sherrell et al., 1999).

The Sm/Fe mass ratios of E271 metalliferous sediments vary in 4.4×10^{-5}–7.9×10^{-5}, which is close to those of sediments from the east side of the EPR near 13°N (4.9×10^{-5}–13.5×10^{-5}, Xue,

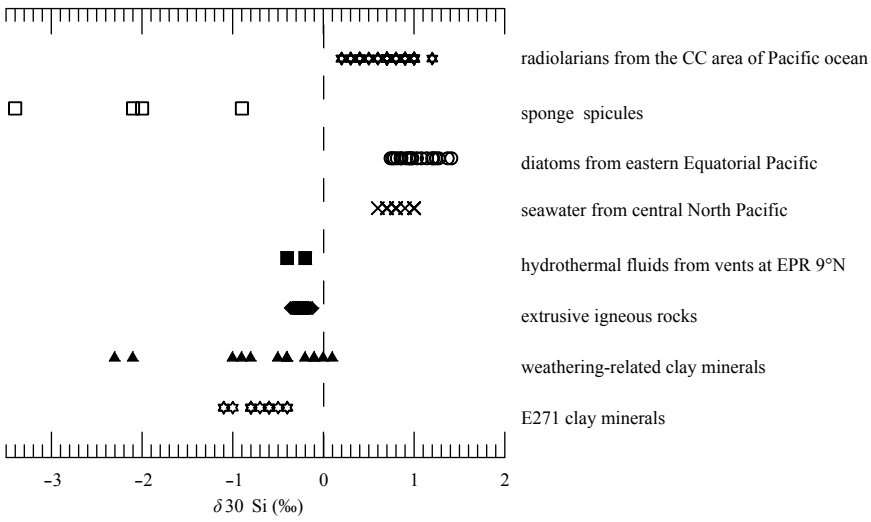

Fig. 9. Graph to show δ^{30}Si values in E271 clay minerals compared with other representative marine and terrestrial examples. Radiolarian data from the CC zone are from Wu et al. (1997), while data on sponge spicules are from Douthitt (1982), data on diatoms from marine sediments in the eastern equatorial Pacific are from Pichevin et al. (2009), seawater data from the central north Pacific and data on hydrothermal vent fluids on the EPR at 9°N are from De La Rocha et al. (2000), data on igneous rocks are from Savage et al. (2013), and data on weathering-related clay minerals are from Douthitt (1982), De La Rocha et al. (2000) and Ziegler et al. (2005).

2003)，but a little lower than those of similar samples from the Southeast Pacific (6.9×10^{-5}–24.1×10^{-5}, Dekov et al., 2010). This difference is the result of the higher REE contents in metalliferous sediments from the southeast compared to the northeast Pacific (Kato et al., 2011), while all samples exhibit higher values than those from hydrothermal plume-particles on the EPR at 13°N and on the EPR at 9°45′N. At the same time, Sm/Fe ratios of E271 clay minerals fall within the range of 0.3×10^{-5}–1.9×10^{-5}, distinctly lower than those of metalliferous sediments, suggesting that Fe-Mn oxide is the main phase that adsorbs REE in these sediments. While the Sm/Fe ratios of E271 clay minerals are higher than those of proximal hydrothermal plume-particles on the EPR at 13°N, these values are nevertheless lower than those of distal hydrothermal particles on the EPR at 9°45′N. These data suggest that E271 clay minerals deplete REE relative to Fe-oxyhydroxide. Similarly, the mean Sm content of terrigenous clay minerals in sediments from the eastern Pacific (10×10^{-6}, Liu et al., 2005) is about five times higher than that of E271 clay minerals (2×10^{-6}); thus, Sm/Fe ratios must also be higher than those of E271 clays, which implies that terrigenous minerals may adsorb more REE than newly formed smectite. Together, all these data suggest that REE are mobilized during the formation of smectite because of a decrease in adsorption capacity, and that the formation of this mineral is the result of reactions between amorphous hydrothermal Fe-oxyhydroxide phases and opal. Finally, a decrease in adsorption capacity may be because the large ionic radii of the REE scavenged by Fe-oxyhydroxide preclude their substitution in either the tetrahedral or octahedral lattice sites of the smectite structure; hence, some are released into solution or lost to other phases (Dymond and Eklund, 1978; Barrett et al., 1986), which results in the depletion of REE in E271 clay minerals.

6 Conclusions

The core E271 sediments collected near the EPR at 13°N comprise amorphous or poorly crystallized Fe-Mn oxides, calcite, clay minerals, quartz, feldspar, and barite, and have high Fe, Mn, and Cu contents, and low Ti and Al contents. The shale-normalized REE distribution patterns of these sediments show obvious Ce anomaly as well as HREE enrichment relative to LREE, implying REE are scavenged from seawater. Together, all these data suggest these samples are typical metalliferous sediments.

Due to the proximity of the North American continent, the clay mineral sources of the E271 metalliferous sediments are complex. We hypothesize that illite, chlorite, and kaolinite are transported from north or central America by rivers or winds, while smectite is rich in Fe, and we suggest almost all smectite is authigenous and likely the result of reactions between hydrothermal Fe-oxyhydroxide, silica, and seawater in metalliferous sediments. The most likely resources of Si for formation is biogenic silica (diatoms and radiolarians), as well as hydrothermal fluids and detrital mineral phases. The formation of authigenic smectite is accompanied by Si isotope fractionation, because preferential adsorption of light Si isotopes onto Fe-oxyhydroxide results in the δ^{30}Si values of newly formed smectite lower than parent SiO_2. Meanwhile, some REE are mobilized during the smectite formation because the large ionic radii of the REE adsorbed by Fe-oxyhydroxide precludes their substitution onto either the tetrahedral or octahedral lattice sites of the smectite structure; thus, some are released into solution or lost to other phases, resulting in the depletion of REE in E271 clay minerals. This implies that the value of metalliferous sediments as a potential resource for REE (Kato et al., 2011) may decrease during the smectite formation.

Acknowledgements

The authors thank the crew of the “DY105-14” cruise for their help with obtaining the samples, as well as the anonymous reviewers for their helpful and valuable comments. The authors are grateful to Li Anchun and Wan Shiming for their help in the X-ray diffraction determination.

References

Alt J C. 1988. Hydrothermal oxide and nontronite deposits on seamounts in the eastern Pacific. Marine Geology, 81(1-4):

227–239
Alt J C, Lonsdale P, Haymon R, et al. 1987. Hydrothermal sulfide and oxide deposits on seamounts near 21°N, East Pacific Rise. Geological Society of America Bulletin, 98(2): 157–168
Antrim L, Sempere J C, Macdonald K C, et al. 1988. Fine scale study of a small overlapping spreading center system at 12°54′N on the East Pacific Rise. Marine Geophysical Researches, 9(2): 115–130
Ballard R D, Hekinian R, Francheteau J. 1984. Geological setting of hydrothermal activity at 12°50′N on the East Pacific Rise: a submersible study. Earth and Planetary Science Letters, 69(1): 176–186
Banks H H Jr. 1972. Iron-rich saponite: additional data on samples dredged from the Mid-Atlantic Ridge, 22°N latitude. Smithsonian Contributions to the Earth Sciences, 9: 39–42
Barrett T J, Friedrichsen H, Fleet A J. 1983. Elemental and stable isotopic composition of some metalliferous and pelagic sediments from the Galapagos mounds area, deep sea drilling project leg 70. In: Honnorez J, Von Herzen R P, eds. Initial Reports of the Deep Sea Drilling Project 70. Washington: U.S. Government Printing Office, 315–323
Barrett T J, Taylor P N, Jarvis I, et al. 1986. Pb and Sr isotope and rare earth element composition of selected metalliferous sediments from sites 597 to 601, Deep Sea Drilling Project Leg 92. In: Leinen M, Rea D K, eds. Initial Reports of the Deep Sea Drilling Project 92. Washington: U.S. Government Printing Office, 391–407
Basile-Doelsch I. 2006. Si stable isotopes in the earth's surface: a review. Journal of Geochemical Exploration, 88(1-3): 252–256
Basile-Doelsch I, Meunier J D, Parron C. 2005. Another continental pool in the terrestrial silicon cycle. Nature, 433(7024): 399–402
Biscaye P E. 1965. Mineralogy and sedimentation of recent deep-sea clay in the Atlantic Ocean and adjacent seas and oceans. Geological Society of America Bulletin, 76(7): 803–832
Bischoff J L. 1972. A ferroan nontronite from the Red Sea geothermal system. Clays and Clay Minerals, 20(4): 217–223
Bonatti E, Kraemer T, Rydell H. 1972. Classification and genesis of submarine iron–manganese deposits. In: Horn D R, ed. Ferromanganese Deposits on the Ocean Floor. Washington D C: National Science Foundation, 149–166
Boström K. 1973. The origin and fate of ferromanganoan active ridge sediments. Stockholm Contributions to Geology, 27(2): 149–243
Buatier M D, Karpoff A M, Boni M, et al. 1994. Mineralogic and petrographic records of sediment-fluid interaction in the sedimentary sequence at Middle Valley, Juan de Fuca Ridge, Leg 139. In: Mottl M J, Davis E E, Fisher A T, et al, eds. Proceedings of the Ocean Drilling Program, Scientific Results, Vol. 139. Ocean Drilling Program: College Station, TX, 133–154
Buatier M D, Karpoff A M, Charpentier D. 2002. Clays and zeolite authigenesis in sediments from the flank of the Juan de Fuca Ridge. Clay Minerals, 37(1): 143–155
Buatier M D, Monnin C, Früh-Green G L, et al. 2001. Fluid-sediment interactions related to hydrothermal circulation in the Eastern Flank of the Juan de Fuca Ridge. Chemical Geology, 175(3-4): 343–360
Butuzova G Y, Drits V A, Lisistyana N A, et al. 1979. Formation dynamics of clay minerals in ore-bearing sediments in the Atlantis II basin, Red Sea. Lithol Miner Resour, 14: 23–32
Carey S, Olsen R, Bell K L C, et al. 2016. Hydrothermal venting and mineralization in the crater of Kick'em Jenny submarine volcano, Grenada (Lesser Antilles). Geochemistry, Geophysics, Geosystems, 17(3): 1000–1019
Chamley H. 1989. Clay Sedimentology. Berlin, Heidelberg: Springer-Verlag, 259–289
Charlou J L, Bougault H, Appriou P, et al. 1991. Water column anomalies associated with hydrothermal activity between 11°40′ and 13°N on the East Pacific Rise: discrepancies between tracers. Deep Sea Research Part A. Oceanographic Research Papers, 38(5): 569–596
Chester R, Hughes M J. 1967. A Chemical technique for the separation of ferro-manganese minerals, carbonate minerals and adsorbed trace elements from pelagic sediments. Chemical Geology, 2: 249–262
Choukroune P, Francheteau J, Hekinian R. 1984. Tectonics of the East Pacific Rise near 12°50′N: a submersible study. Earth and Planetary Science Letters, 68(1): 115–127
Cole T G. 1985. Composition, oxygen isotope geochemistry and origin of smectite in the metalliferous sediments of the Bauer Deep, southeast Pacific. Geochimica et Cosmochimica Acta, 49(1): 221–235
Cole T G. 1988. The nature and origin of smectite in the Atlantis II Deep, Red Sea. The Canadian Mineralogist, 26(3): 755–763
Cole T G, Shaw H F. 1983. The nature and origin of authigenic smectites in some recent marine sediments. Clay Minerals, 18(3): 239–252
Crane K. 1987. Structural evolution of the east pacific rise axis from 13°10′N to 10°35′N: interpretations from SeaMARC I data. Tectonophysics, 136(1-2): 65–124
Cuadros J, Dekov V M, Arroyo X, et al. 2011. Smectite formation in submarine hydrothermal sediments: samples from the HMS challenger expedition (1872-1876). Clays and Clay Minerals, 59(2): 147–164
Davydov M P, Sudarikov S M, Aleksandrov P A, et al. 2002. Geochemistry of the metalliferous sediments of hydrothermal fields of the east pacific rise, 11°30′-13°N. Part 1. Geochemistry of Holocene Sediments. Geochemistry International, 40(3): 279–298
De Baar H J W, Bacon M P, Brewer P G, et al. 1985. Rare earth elements in the pacific and Atlantic Oceans. Geochimica et Cosmochimica Acta, 49(9): 1943–1959
De La Rocha C L, Brzezinski M A, DeNiro M J, et al. 1998. Silicon-isotope composition of diatoms as an indicator of past oceanic change. Nature, 395(6703): 680–683
De La Rocha C L, Brzezinski M A, DeNiro M J. 2000. A first look at the distribution of the stable isotopes of silicon in natural waters. Geochimica et Cosmochimica Acta, 64(14): 2467–2477
Dekov V M, Cuadros J, Kamenov G D, et al. 2010. Metalliferous sediments from the H. M.S. *Challenger* voyage (1872-1876). Geochimica et Cosmochimica Acta, 74(17): 5019–5038
Dekov V M, Cuadros J, Shanks W C, et al. 2008. Deposition of talc-kerolite-smectite-smectite at seafloor hydrothermal vent fields: evidence from mineralogical, geochemical and oxygen isotope studies. Chemical Geology, 247(1–2): 171–194
Demarest M S, Brzezinski M A, Beucher C P. 2009. Fractionation of silicon isotopes during biogenic silica dissolution. Geochimica et Cosmochimica Acta, 73(19): 5572–5583
Ding Tiping, Jiang Shaoyong, Wan Defang, et al. 1996. Silicon Isotope Geochemistry. Beijing: Geological Publishing House
Douthitt C B. 1982. The geochemistry of the stable isotopes of silicon. Geochimica et Cosmochimica Acta, 46(8): 1449–1458
Douville E, Bienvenu P, Charlou J L, et al. 1999. Yttrium and rare earth elements in fluids from various deep-sea hydrothermal systems. Geochimica et Cosmochimica Acta, 63(5): 627–643
Dunk R M, Mills R A. 2006. The impact of oxic alteration on plume-derived transition metals in ridge flank sediments from the East Pacific Rise. Marine Geology, 229(3–4): 133–157
Dymond J, Eklund W. 1978. A microprobe study of metalliferous sediment components. Earth and Planetary Science Letters, 40(2): 243–251
Fouquet Y, Auclair G, Cambon P, et al. 1988. Geological setting and mineralogical and geochemical investigations on sulfide deposits near 13°N on the East Pacific Rise. Marine Geology, 84(3–4): 145–178
Francheteau J, Ballard R D. 1983. The East Pacific Rise near 21°N, 13°N and 20°S: inferences for along-strike variability of axial processes of the mid-ocean ridge. Earth and Planetary Science Letters, 64(1): 93–116
Gablina I F, Popova E A, Sadchikova T A, et al. 2014. Hydrothermal metasomatic alteration of carbonate bottom sediments in the Ashadze-1 field (13°N Mid-Atlantic Ridge). Geology of Ore Deposits, 56(5): 357–379
Georg R B, Zhu C, Reynolds B C, et al. 2009. Stable silicon isotopes of groundwater, feldspars, and clay coatings in the Navajo Sandstone aquifer, Black Mesa, Arizona, USA. Geochimica et

Cosmochimica Acta, 73(8): 2229–2241
German C R, Colley S, Palmer M R, et al. 2002. Hydrothermal plume-particle fluxes at 13°N on the East Pacific Rise. Deep Sea Research Part I: Oceanographic Research Papers, 49(11): 1921–1940
German C R, Klinkhammer G P, Edmond J M, et al. 1990. Hydrothermal scavenging of rare-earth elements in the ocean. Nature, 345(6275): 516–518
Griffin J J, Windom H, Goldberg E D. 1968. The distribution of clay minerals in the world ocean. Deep Sea Research and Oceanographic Abstracts, 15(4): 433–459
Grill E V, Chase R L, MacDonald R D, et al. 1981. A hydrothermal deposit from explorer ridge in the northeast Pacific Ocean. Earth and Planetary Science Letters, 52(1): 142–150
Gurvich E G. 2006. Metalliferous Sediments of the World Ocean: Fundamental Theory of Deep-Sea Hydrothermal Sedimentation. Berlin: Springer, 1–126
Haskin M A, Haskin L A. 1966. Rare earths in European shales: a redetermination. Science, 154(3748): 507–509
Heath G R, Dymond J. 1977. Genesis and transformation of metalliferous sediments from the East Pacific Rise, Bauer Deep, and Central Basin, northwest Nazca plate. Geological Society of America Bulletin, 88(5): 723–733
Hein J R, Scholl D W. 1978. Diagenesis and distribution of late Cenozoic volcanic sediment in the southern Bering Sea. Geological Society of America Bulletin, 89(2): 197–210
Hein J R, Yeh H W, Alexander E. 1979. Origin of iron-rich montmorillonite from the manganese nodule belt of the north equatorial Pacific. Clays and Clay Minerals, 27(3): 185–194
Hekinian R, Fouquet Y. 1985. Volcanism and metallogenesis of axial and off-axial structures on the East Pacific Rise near 13 degrees N. Economic Geology, 80(2): 221–249
Hekinian R, Fevrier M, Avedik F, et al. 1983a. East Pacific Rise near 13°N: geology of new hydrothermal fields. Science, 219(4590): 1321–1324
Hekinian R, Fevrier M, Bischoff J L, et al. 1980. Sulfide deposits from the East Pacific Rise near 21°N. Science, 207(4438): 1433–1444
Hekinian R, Francheteau J, Renard V, et al. 1983b. Intense hydrothermal activity at the axis of the east pacific rise near 13°N: sumbersible witnesses the growth of sulfide chimney. Marine Geophysical Researches, 6(1): 1–14
Hoffert M, Karpoff A M, Schaaf A, et al. 1981. The sedimentary deposits of the tiki basin (south-east pacific) passage from carbonate oozes to “metalliferous sediments”. In: Lalou C, ed. Colloques Internationaux du Centre National de la Recherche Scientifique. Paris: CNRS, 289. 101–112
Honnorez J, Karpoff A M, Trauth-Badaut D. 1983. Sedimentology, mineralogy, and geochemistry of green clay samples from the Galapagos hydrothermal mounds, holes 506, 506C, and 507D, deep sea drilling project leg 70 (preliminary data). In: Honnorez J, Von Herzen R P, eds. Initial Reports of the Deep Sea Drilling Project 70. Washington: U.S. Government Printing Office, 211–224
Hovan S A. 1995. Late Cenozoic atmospheric circulation intensity and climatic history recorded by eolian deposition in the eastern equatorial Pacific, Leg 138. In: Pisias N G, Mayer L A, Janecek T R, et al, eds. Proceedings of the Ocean Drilling Program, Scientific Results, Vol. 138. Ocean Drilling Program: College Station, TX, 615–625
Huang Jie, Wan Shiming, Xiong Zhifang, et al. 2016. Geochemical records of Taiwan-sourced sediments in the South China Sea linked to Holocene climate changes. Palaeogeography, Palaeoclimatology, Palaeoecology, 441: 871–881
Kadko D. 1985. Late Cenozoic sedimentation and metal deposition in the North Pacific. Geochimica et Cosmochimica Acta, 49(3): 651–661
Kato Y, Fujinaga K, Nakamura K, et al. 2011. Deep-sea mud in the Pacific Ocean as a potential resource for rare-earth elements. Nature Geoscience, 4(8): 535–539
Klitgord K D, Mammerickx J. 1982. Northern East Pacific Rise: magnetic anomaly and bathymetric framework. Journal of Geophysical Research: Solid Earth, 87(B8): 6725–6750
Lackschewitz K S, Botz R, Garbe-Schönberg D, et al. 2006. Mineralogy and geochemistry of clay samples from active hydrothermal vents off the north coast of Iceland. Marine Geology, 225(1-4): 177–190
Lackschewitz K S, Singer A, Botz R, et al. 2000. Formation and transformation of clay minerals in the hydrothermal deposits of Middle Valley, Juan de Fuca Ridge, ODP Leg 169. Economic Geology, 95(2): 361–389
Lalou C, Brichet E, Hekinian R. 1985. Age dating of sulfide deposits from axial and off-axial structures on the East Pacific Rise near 12°50′N. Earth and Planetary Science Letters, 75(1): 59–71
Leinen M, Prospero J M, Arnold E, et al. 1994. Mineralogy of Aeolian dust reaching the North Pacific Ocean: 1. Sampling and analysis. Journal of Geophysical Research: Atmospheres, 99(D10): 21017–21023
Lisitzin A P, Bogdanov Y A, Mudmaa I O, et al. 1976. Metalliferous sediments and their genesis. In: Lisitzin A P, ed. Geological and Geophysical Research in the Southeast Pacific (in Russian). Moscow: Nauka, 289–379
Liu Hanbin, Jin Guishan, Li Junjie, et al. 2013. Determination of stable isotope composition in uranium geological samples. World Nuclear Geoscience (in Chinese), 30(3): 174–179
Liu Jihua, Shi Xuefa, Chen Lirong, et al. 2005. REE and ε_{Nd} of clay fractions in sediments from the eastern Pacific Ocean: evidence for clay sources. Science in China Series D: Earth Sciences, 48(5): 701–712
Lyle M, Dymond J, Heath G R. 1977. Copper-nickel-enriched ferromanganese nodules and associated crusts from the Bauer Basin, northwest Nazca plate. Earth and Planetary Science Letters, 35(1): 55–64
McMillen K J, Enkeboll R H, Moore J C, et al. 1982. Sedimentation in different tectonic environments of the Middle America Trench, southern Mexico and Guatemala. Geological Society, London, Special Publications, 10(1): 107–119
McMurtry G M, Yeh H W. 1981. Hydrothermal clay mineral formation of East Pacific Rise and Bauer Basin sediments. Chemical Geology, 32(1–4): 189–205
Melson W G, Thompson G. 1973. Glassy abyssal basalts, Atlantic sea floor near St. Paul’s Rocks: petrography and composition of secondary clay minerals. Geological Society of America Bulletin, 84(2): 703–716
Mills R A, Elderfield H. 1995. Hydrothermal activity and the geochemistry of metalliferous sediment. In: Humphris S E, Zierenberg R A, Mullineaux L S, et al, eds. Seafloor Hydrothermal Systems: Physical, Chemical, Biological, and Geological Interactions. Washington D C: American Geophysical Union, 392–407
Miyoshi Y, Ishibashi J, Shimada K, et al. 2015. Clay minerals in an active hydrothermal field at Iheya-North-Knoll, Okinawa trough. Resource Geology, 65(4): 346–360
Murnane R, Clague D A. 1983. Nontronite from a low-temperature hydrothermal system on the Juan de Fuca Ridge. Earth and Planetary Science Letters, 65(2): 343–352
Opfergelt S, Cardinal D, André L, et al. 2010. Variations of δ^{30}Si and Ge/Si with weathering and biogenic input in tropical basaltic ash soils under monoculture. Geochimica et Cosmochimica Acta, 74(1): 225–240
Opfergelt S, de Bournonville G, Cardinal D, et al. 2009. Impact of soil weathering degree on silicon isotopic fractionation during adsorption onto iron oxides in basaltic ash soils, Cameroon. Geochimica et Cosmochimica Acta, 73(24): 7226–7240
Percival J B, Ames D E. 1993. Clay mineralogy of active hydrothermal chimneys and an associated mound, middle valley, northern Juan de Fuca ridge. The Canadian Mineralogist, 31(4): 957–971
Peter J M, Scott S D. 1988. Mineralogy, composition, and fluid-inclusion microthermometry of seafloor hydrothermal deposits in the southern trough of Guaymas Basin, Gulf of California. The Canadian Mineralogist, 26(3): 567–587
Pichevin L E, Reynolds B C, Ganeshram R S, et al. 2009. Enhanced carbon pump inferred from relaxation of nutrient limitation in the glacial ocean. Nature, 459(7250): 1114–1117

Piper D Z. 1974. Rare earth elements in the sedimentary cycle: a summary. Chemical Geology, 14(4): 285–304

Piper D Z, Heath G R. 1989. Hydrogenous sediment. In: Winterer E L, Hussong D M, Decker R W, eds. The Eastern Pacific Ocean and Hawaii. the Geology of North America, Vol. N. Boulder, Colorado: Geological Society of America, 337–345

Rateev M A, Timofeev P P, Rengarten N V. 1980. Minerals of the clay fraction in Pliocene-Quaternary sediments of the east equatorial Pacific. In: Rosendahl B R, Hekinian R, Natland J H, et al, eds. Init Repts DSDP 54, Washington: U.S. Government Printing Office, 307-318

Savage P S, Georg R B, Williams H M, et al. 2013. The silicon isotope composition of the upper continental crust. Geochimica et Cosmochimica Acta, 109: 384–399

Scheidegger K F, Stakes D S. 1977. Mineralogy, chemistry and crystallization sequence of clay minerals in altered tholeiitic basalts from the Peru Trench. Earth and Planetary Science Letters, 36(3): 413–422

Schumann D, Nagel U. 1982. Appendix I. X-ray mineralogical analysis. In: Initial Reports of the Deep Sea Drilling Project 66. Washington: U.S. Government Printing Office, 853–857

Seyfried Jr W E, Shanks III W C, Dibble Jr W E. 1978. Clay mineral formation in DSDP Leg 34 basalt. Earth and Planetary Science Letters, 41(3): 265–276

Shao Hebin, Yang Shouye, Wang Quan, et al. 2015. Discriminating hydrothermal and terrigenous clays in the Okinawa Trough, East China Sea: evidences from mineralogy and geochemistry. Chemical Geology, 398: 85–96

Sharaskin A Y, Migdisov A A, Rostschina I A, et al. 1983. Major-and trace-element chemistry of hole 504B basalts and their alteration products (costa Rica rift, deep sea drilling project leg 70). In: Cann J R, Langseth M G, Honnorez J, et al, eds. Initial Reports Deep Sea Drilling Proiect 69. Washington: U.S. Government Printing Office, 775–789

Sherrell R M, Field M P, Ravizza G. 1999. Uptake and fractionation of rare earth elements on hydrothermal plume particles at 9°45′N, East Pacific Rise. Geochimica et Cosmochimica Acta, 63(11-12): 1709–1722

Varela D E, Pride C J, Brzezinski M A. 2004. Biological fractionation of silicon isotopes in Southern Ocean surface waters. Global Biogeochemical Cycles, 18(1): GB1047

Wan Shiming, Li Anchun, Clift P D, et al. 2007. Development of the East Asian monsoon: mineralogical and sedimentologic records in the northern South China Sea since 20 Ma. Palaeogeography, Palaeoclimatology, Palaeoecology, 254(3-4): 561–582

Wan Shiming, Li Anchun, Clift P D, et al. 2010. Increased contribution of terrigenous supply from Taiwan to the northern South China Sea since 3 Ma. Marine Geology, 278(1-4): 115–121

Wang Xiaoyuan, Yin Xuebo, Zeng Zhigang, et al. 2014. High efficiency determination of trace elements in the geological samples. Journal of Chinese Mass Spectrometry Society (in Chinese), 35(1): 24–31

Wu Li. 2012. Study on the metalliferous sediments near 13°N East Pacific Rise (in Chinese) [dissertation]. Qingdao: Institute of Oceanology Chinese Academy of Sciences

Wu Shiying, Ding Tiping, Meng Xianwei, et al. 1997. Determination and geological implication of O-Si isotope of the sediment core in the CC area, the Pacific Ocean. Chinese Science Bulletin, 42(17): 1462–1465

Xue Fayu. 2003. Geochemical study of the sediments from two cores in the hydrothermal field on the East Pacific Rise (in Chinese) [dissertation]. Qingdao: Ocean University of China

Yu Shaoxiong. 2010. Total organic carbon and nitrogen from metalliferous sediment on the flank of the East Pacific Rise 13°N (in Chinese) [dissertation]. Qingdao: Institute of Oceanology Chinese Academy of Sciences

Yu Zenghui, Gao Yuhua, Zhai Shikui, et al. 2012. Resolving the hydrothermal signature by sequential leaching studies of sediments from the middle of the Okinawa Trough. Science China Earth Sciences, 55(4): 665–674

Yuan Chunwei, Zeng Zhigang, Yin Xuebo et al. 2007. Sediment geochemistry from 13°N East Pacific Rise hydrothermal field. Marine Geology & Quaternary Geology (in Chinese), 27(4): 45–53

Zhang Guoliang, Zeng Zhigang, Yin Xuebo, et al. 2008. Periodical mixing of MORB magmas near East Pacific Rise 13°N: evidence from modeling and zoned plagioclase phenocrysts. Science in China Series D: Earth Sciences, 51(12): 1786–1801

Ziegler K, Chadwick O A, Brzezinski M A, et al. 2005. Natural variations of δ^{30}Si ratios during progressive basalt weathering, Hawaiian Islands. Geochimica et Cosmochimica Acta, 69(19): 4597–4610

Zierenberg R A, Shanks III W C. 1994. Sediment alteration associated with massive sulfide formation in Escanaba Trough, Gorda Ridge: the importance of seawater mixing and magnesium metasomatism. In: Morton J L, Zierenberg R A, Reiss C A, eds. Geologic, Hydrothermal, and Biologic Studies at Escanaba Trough, Gorda Ridge, Offshore Northern California. Commonwealth of Virginia: US Geological Survey, 2022: 257–277